

# High bandwidth underwater optical communication

Frank Hanson<sup>1,\*</sup> and Stojan Radic<sup>2</sup>

<sup>1</sup>Space and Naval Warfare Systems Center, San Diego, California 92152, USA

<sup>2</sup>Department of Electrical and Computer Engineering, University of California San Diego, San Diego, California 92093-0407, USA

\*Corresponding author: hansonfe@spawar.navy.mil

Received 24 October 2007; revised 28 November 2007; accepted 30 November 2007;  
posted 3 December 2007 (Doc. ID 88958); published 9 January 2008

We report error-free underwater optical transmission measurements at 1 Gbit/s ( $10^9$  bits/s) over a 2 m path in a laboratory water pipe with up to 36 dB of extinction. The source at 532 nm was derived from a 1064 nm continuous-wave laser diode that was intensity modulated, amplified, and frequency doubled in periodically poled lithium niobate. Measurements were made over a range of extinction by the addition of a  $\text{Mg}(\text{OH})_2$  and  $\text{Al}(\text{OH})_3$  suspension to the water path, and we were not able to observe any evidence of temporal pulse broadening. Results of Monte Carlo simulations over ocean water paths of several tens of meters indicate that optical communication data rates  $>1$  Gbit/s can be supported and are compatible with high-capacity data transfer applications that require no physical contact. © 2008 Optical Society of America

OCIS codes: 010.04455, 010.4458, 060.2605, 060.4510, 190.0190, 290.7050.

## 1. Introduction

This work was motivated by a need to demonstrate error-free underwater communication at qualitatively higher data rates than previously reported with either optical or acoustic methods. There is an increasing emphasis on monitoring the ocean environment for scientific, commercial, and military reasons [1–3], and communication between various underwater vehicles and sensors is essential. Underwater sensors are often deployed in remote locations and can collect data over long periods of time. The volume of stored data can be large and should be expected to grow as sensor technology becomes more complex. Although techniques for underwater acoustic communication are well established and practical in many cases, we envision situations where it might be useful to send information using free-space optical links. Acoustic transmission is possible over ranges of many kilometers, but optical communication has the potential to provide data rates that are higher than acoustic rates by orders of magnitude. Acoustic transmission becomes increasingly difficult at higher carrier frequency due to absorption and multipath effects. Power absorption increases as the square of

the frequency and is greater than 30 dB/m at 10 MHz [4]. In contrast, optical propagation is affected by absorption and scattering, with magnitudes that can vary widely in different ocean water types [5–7]. It is important to understand how water conditions might affect the performance of optical communication at high data rates. In clean ocean water, transmission is optimum in the blue–green spectral region. In these environments the absorption and volume scattering coefficients,  $a$  and  $b$ , can approach  $0.1 \text{ m}^{-1}$  [7]. Scattering will reduce signal levels but also can limit the maximum data rate when temporal pulse stretching due to multipath effects is comparable to the bit time. This will depend on a variety of geometric factors in addition to water quality, including source beam divergence, propagation distance, receiver field of view, and source beam misalignment.

In recent years there have been several studies that have addressed the potential capabilities of optical underwater communication systems [7–10], and some notable demonstrations at high data rates have been published. Some early experiments demonstrated data rates up to 50 Mbits/s in seawater over a 9 m path (5.1 attenuation lengths) using an argon-ion laser operating at 514 nm and a bulk electro-optic (EO) modulator [11]. More recent work demonstrated transmission of pulse trains at up to a 10 MHz rep-

etition rate with light emitting diodes in a 91 m water tank test [12].

Underwater optical propagation experiments are commonly done with simulated conditions in a laboratory water tank because of the difficulty associated with performing experiments in the ocean that require stable platforms. Although laboratory propagation ranges are necessarily limited, the water conditions can be controlled so that the total scattering and absorption are comparable to a much longer range in the ocean. In fact, it should be possible to achieve optical radiance in a tank that is a scaled version of what might be expected for longer ranges in an ocean environment. For these purposes, water is characterized by an absorption coefficient  $a$  ( $\text{m}^{-1}$ ) and volume scattering function  $\beta(\theta)$  ( $\text{m}^{-1} \text{sr}^{-1}$ ), and the total integrated scattering coefficient  $b$  ( $\text{m}^{-1}$ ) is given by

$$b = 2\pi \int_0^\pi \sin(\theta) \beta(\theta) d\theta. \quad (1)$$

The optical radiance  $L(\mathbf{r}, \mathbf{s}, t)$  (in units of  $\text{W m}^{-2} \text{sr}^{-1}$ ), which is the radiant flux at  $\mathbf{r}$  propagating in the direction of the unit vector  $\mathbf{s}$ , is a solution to the time-dependent radiative transport equation [13]:

$$\begin{aligned} \frac{1}{v} \frac{\partial}{\partial t} L(\mathbf{r}, \mathbf{s}, t) + \mathbf{s} \cdot \nabla L(\mathbf{r}, \mathbf{s}, t) \\ = -\rho \sigma L(\mathbf{r}, \mathbf{s}, t) + \int_{4\pi} \beta(\theta) L(\mathbf{r}, \mathbf{s}', t) d\mathbf{s}'. \end{aligned} \quad (2)$$

Here,  $v$  is the speed of light,  $\sigma$  is the total cross section for absorption and scattering,  $\rho\sigma = a + b$ , and  $\theta$  is the angle between the directions  $\mathbf{s}'$  and  $\mathbf{s}$ . It is evident that if  $L(\mathbf{r}, \mathbf{s}, t)$  is a solution to Eq. (2) in water that is characterized by  $a_0$  and  $\beta_0(\theta)$ , then the scaled radiance  $L(f\mathbf{r}, \mathbf{s}, ft)$  is a solution in water where the density  $\rho$  of absorbing and scattering particles is scaled by  $f$  so that  $a = fa_0$  and  $\beta(\theta) = f\beta_0(\theta)$ . This simple scaling can be verified by multiplying Eq. (2) by  $f$  and making the substitutions  $\mathbf{r} \rightarrow f\mathbf{r}$  and  $t \rightarrow ft$ . While the angular intensity distributions are preserved, the spatial and time scales are reduced by the factor  $f$ . We are neglecting the (usually minor) effects of turbulence and large-scale refractive index fluctuations in the ocean that are not simulated in the laboratory tank. In practice, the laboratory experiments are not exact scaled representations, because some light will interact with the tank walls. The water-pipe geometry used in these experiments and the effort made to reduce wall effects will be described below.

Since a general analytical solution to the radiative transport equation [Eq. (2)] is not available and the modeling of underwater optical propagation is approximate, Monte Carlo simulations are often used to provide details for a specific optical geometry [6]. They can give an accurate representation of an experiment to within their statistical limits if the cor-

rect volume scattering function and absorption are used. They can also be used to predict temporal effects such as pulse broadening [14], which may be difficult to measure. A series of these simulations were performed to compare with the laboratory results. Simulations were also performed for propagation over longer ranges and in more realistic ocean conditions, and the implications for high data rate communication in these environments are discussed.

## 2. Experimental

Although continuous-wave (cw) green sources are readily available, they cannot be easily modulated at high frequency. To provide an optical waveform modulated at gigabits per second or higher rates, an indirect approach, shown schematically in Fig. 1, was used. A single-frequency, single-mode cw 1064 nm laser diode (LD) provided  $\sim 10$  mW (10 dBm) of power that was launched via an optical isolator and polarization controller (Pol) into a lithium niobate waveguide EO amplitude modulator (EO mod). Each component was pigtailed using an equivalent of Flex-core (980 nm) optical fiber to guarantee an absence of parasitic multiple path interference prior to frequency doubling. The 20 GHz bandwidth modulator was biased to achieve  $\sim 100\%$  amplitude modulation and driven by low-voltage pseudorandom, non-return-to-zero  $2^{10}$  length bit sequence at 1 Gbit/s generated by an HP model 70843B bit error ratio tester. This waveform was then amplified to  $\sim 30$  dBm of average power in a ytterbium-doped fiber amplifier (YDFA), which maintained linear polarization. The amplified signal was then frequency doubled to 532 nm in periodically poled lithium niobate (PPLN) heated to  $\sim 180^\circ\text{C}$  for the correct phase matching and reduction of its inherent susceptibility of photorefractive damage. The pump light was focused into the 1 cm long PPLN crystal in a nearly confocal geometry with a waist radius at  $1/e^2$  intensity of  $\sim 37 \mu\text{m}$ , which should give close to optimum conversion [15]. The crystal aperture was  $0.5 \text{ mm} \times 0.5 \text{ mm}$ . The conversion efficiency was found to have a quadratic dependence on pump power as ex-

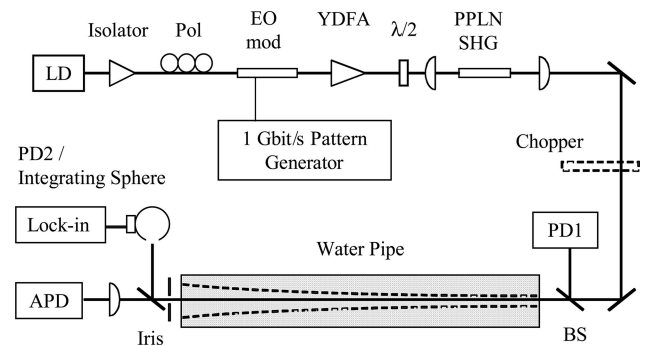


Fig. 1. Experimental layout for optical propagation through the 2 m water pipe. Pol is polarization control, EO mod is a lithium niobate waveguide amplitude modulator, YDFA is a ytterbium-doped fiber amplifier,  $\lambda/2$  is a half-wave plate, and PD are photodiode detectors.

pected from a single-frequency doubling process in  $\chi^{(2)}$  material. A maximum of 7.7 mW (8.9 dBm) of average power at 532 nm was obtained in a 25% duty-factor waveform with 0.9 W (29.5 dBm) of average pump power at 1064 nm. The amplitude modulation was essentially 100%. No degradations with photorefractive damage were observed during the measurements.

A diagram of the experimental layout is shown in Fig. 1. The 532 nm frequency-doubled light from the PPLN crystal was collimated to an  $\sim 1$  mm beam radius, the fundamental was removed with a high-reflecting mirror at 1064 nm, and the beam was directed down the axis of the 2 m water pipe. This pipe was constructed from a 4 in. inside diameter acrylonitrile butadiene styrene (ABS) plastic with 2 in. diameter fused silica windows at either end. To reduce any parasitic light scattering from the inside wall, a layer of black mesh filter cloth was cemented to the inside wall of the pipe. The bare pipe wall was smooth and gave a strong specular reflection, but the mesh cloth was judged to significantly reduce the reflectivity. Hose fittings near each end allowed water circulation through an external pump. The pipe was filled to nearly full capacity ( $\sim 16$  l) with pure water generated by reverse osmosis. During the course of the experiment, only a small to no air/water interface was present inside the pipe volume. Water was circulated through the pipe and filtered for a period of time to begin the experiment with "clean" water conditions.

The average power incident on the water column ranged up to 7.3 mW (8.6 dBm), and a small part of this beam was split off and directed to a photodiode (PD1) to monitor incident power. An iris was placed just after the exit window of the pipe to control the transmission of scattered light. A beam splitter (BS) directed a fixed fraction of the light into an integrating sphere and photodiode (PD2) to measure the intensity of the light transmitted through the water pipe. During the transmission measurements, a chopper was placed in the incident beam and a lock-in amplifier was used. The signal from the integrating sphere was calibrated to measure internal water-pipe transmission by moving the water pipe outside of the beam line and correcting for transmission of the windows. The 1 in. (2.54 cm) aperture of the integrating sphere had a half-angle field of view of  $\sim 100$  mrad from the end of the water column and subtended  $\sim 0.01\pi$  sr. Light passing through the iris and BS was focused onto a 1 GHz bandwidth avalanche photodiode detector (APD) with a 5 cm lens. The relevant specifications for this detector (Menlo Systems Model APD-210) are 0.5 mm active diameter,  $\sim 15$  A/W response at 532 nm at a gain of 100, and noise equivalent power (NEP) of  $0.4$  pW/Hz $^{1/2}$ . The half-angle field of view of the detector-lens combination was 5 mrad.

Volume scattering in the water was created with suspensions of  $\text{Al}(\text{OH})_3$  and  $\text{Mg}(\text{OH})_2$  that were obtained by adding a commercial antacid preparation

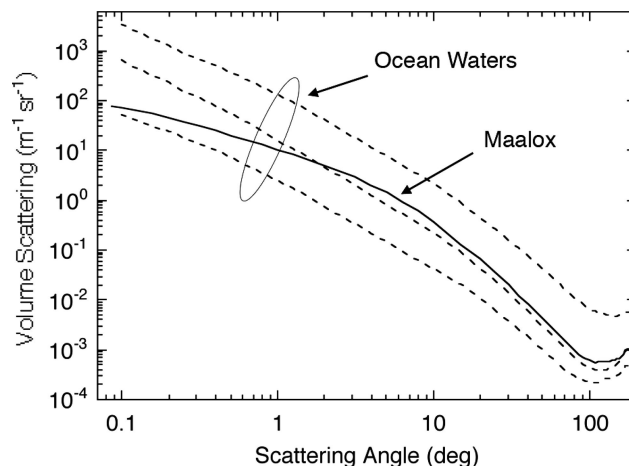


Fig. 2. Volume scattering functions from [17] for three types of ocean water (dashed curves, from top): harbor water, coastal ocean, and clear ocean, and Maalox (solid curve). The Maalox data have been scaled by 0.399 to give the same integrated scattering coefficient,  $b = 0.220 \text{ m}^{-1}$ , as the coastal ocean water.

(Maalox). This approach is commonly used in laboratory experiments to provide scattering [16]. Other minor constituents in the mixture are soluble in water. Petzold [17] has measured the volume scattering function  $\beta(\theta)$  of diluted Maalox and several ocean water types including three that can be characterized as "clear ocean," "coastal ocean," and "harbor water," and these scattering functions are shown in Fig. 2. The scattering measurements were made in a spectral band centered at  $\lambda \sim 515$  nm and with  $\sim 75$  nm full width at half-maximum. The angular dependence of  $\beta(\theta)$  in the three ocean water types is similar, but the magnitudes range over almost a factor of 100. The measurements for Maalox were for an unspecified concentration, and therefore the volume scattering function plotted in Fig. 2 has been scaled by 0.399 in order to give the same integrated scattering value as the coastal ocean water,  $b = 0.220 \text{ m}^{-1}$ . There is significantly less small angle scattering in the Maalox suspensions than in these ocean waters due to the different particle size distributions. Measured values of the absorption  $a$ , total scattering  $b$ , and extinction  $c = a + b$  are listed in Table 1, but it should be noted that the absorption measurements were made in a spectral band centered at  $\lambda \sim 530$  nm.

Table 1. Optical Properties for Three Ocean Water Types and Maalox from [17]

Water Type	$a$ ( $\text{m}^{-1}$ )	$b$ ( $\text{m}^{-1}$ )	$c$ ( $\text{m}^{-1}$ )
Clear ocean <sup>a</sup>	0.114	0.0374	0.1514
Coastal ocean <sup>b</sup>	0.179	0.220	0.399
Harbor water <sup>c</sup>	0.366	1.829	2.195
Maalox suspension <sup>d</sup>	0.055	0.220	0.275

<sup>a</sup>Bahamas (station 8, Tongue of the Ocean, 1.6 km deep).

<sup>b</sup>Catalina channel (station 11).

<sup>c</sup>San Diego Harbor (station 2040).

<sup>d</sup>Scaled by 0.399.



The experiment began with clean water, and the external particulate filter was removed from the pump line. The water transmission in the pipe, internal to the windows, was initially 0.59 or  $-2.3$  dB. A quantity of  $\sim 1\%$  diluted Maalox was prepared, and portions of a few milliliters were added in steps to the water in the pipe. After each step the water was circulated for a few minutes to obtain a uniform scattering suspension. The total transmission as a function of iris aperture was measured at several levels of scattering. The aperture diameter varied from 7.5 to 20.5 mm, corresponding to an aperture half-angle, defined as aperture radius divided by the 2 m path length, that varied from 1.9 to 5.1 mrad, although larger scattering angles would be transmitted from scattering events closer to the iris. In all cases the aperture diameter was large compared to the incident beam diameter. The transmission through the smallest iris setting varied from  $-2.2$  to  $-36$  dB during the experiment as the scattering in the water was increased. As expected, the transmission was more sensitive to aperture size as scattering became stronger.

After each addition of Maalox, bit error ratio measurements were taken from the APD signal using a standard telecom error counter (HP Model 70843B) and eye diagrams were recorded with a high-bandwidth sampling oscilloscope. Although some fi-

nite temporal pulse broadening was surely present because of multiple photon paths from scattering in the water, we were not able to observe any evidence of broadening within the time resolution of our instruments (combination of 1 GHz APD and 40 GHz oscilloscope). Error-free ( $<10^{-9}$ ) detection was achieved as the scattering increased, by increasing the incident optical power. This was accomplished by first removing some attenuation and later by increasing the gain of the YDFA. Representative eye diagrams at 0.045 mW ( $-13$  dBm) incident power with  $-7$  dB extinction and 7.3 mW (8.6 dBm) incident power with  $-36$  dB extinction are shown in Fig. 3. Error-free detection was achieved with up to  $-36$  dB of extinction, limited by the expected reliability of the PPLN crystal at this power. The receiver noise was found to scale linearly with the signal level and was much larger than the specified APD noise of  $\sim 10$   $\mu$ V in a 1 GHz bandwidth. We believe the noise was dominated by transmitter power fluctuations. These could have arisen from low frequency mechanical vibrations that affected the SHG conversion in the tightly focused 1  $\mu$ m pump beam.

### 3. Monte Carlo Calculations

Monte Carlo calculations were performed with standard techniques [6] to model optical propagation in the experimental geometry. We give here a brief description of the approach. The probability density of a photon traveling a distance  $\zeta$  without scattering was mapped onto a random variable  $x$  in the unit interval from 0 to 1 according to  $x = 1 - \exp(-b\zeta)$ , which results in a random scattering distance generator  $\zeta(x) = -\log(1 - x)/b$ . A random scattering angle generator  $\theta(x)$  was constructed in a similar way by mapping the integrated probability distribution onto a random variable  $x$  in the unit interval from 0 to 1:

$$x = \frac{2\pi}{b} \int_0^\theta \beta(\theta') \sin(\theta') d\theta'. \quad (3)$$

Finally, the azimuthal angle  $\phi$  of the scattering direction has a uniform distribution from 0 to  $2\pi$ , and the generator was  $\phi(x) = 2\pi x$ . Each photon was launched with an initial ray direction along the center axis of the water pipe. A random number was used to determine the distance before scattering. Two more random numbers were then used to obtain the polar and azimuthal scattering angles in the coordinate system of the current ray direction. This procedure was repeated until the photon crossed a boundary defined by a cylinder with a length of 2 m and chosen radius. If the photon hit the end plane, the position, incident angle, total path length  $\xi$ , and intensity equal to  $\exp(-a\xi)$  were saved. Results will be described for two sets of cylindrical boundary conditions: a set with a cylinder radius of 5 cm corresponding to the experimental geometry, and another set with a radius of 1 m that effectively represents no radial boundary.

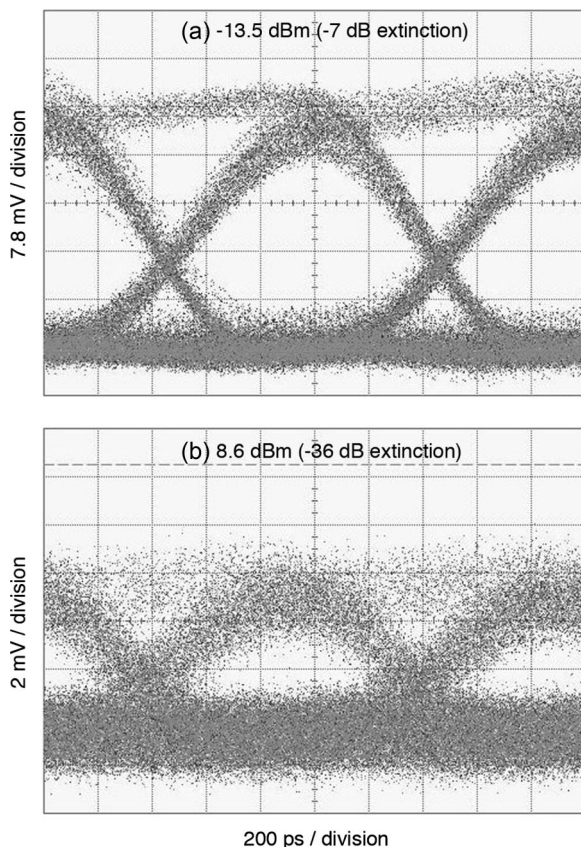


Fig. 3. Representative eye diagrams for the 1 Gbit/s and 25% density waveform transmitted through the water pipe with average power of (a) 0.045 mW and (b) 7.3 mW, and water path extinction of  $-7$  and  $-36$  dB, respectively.

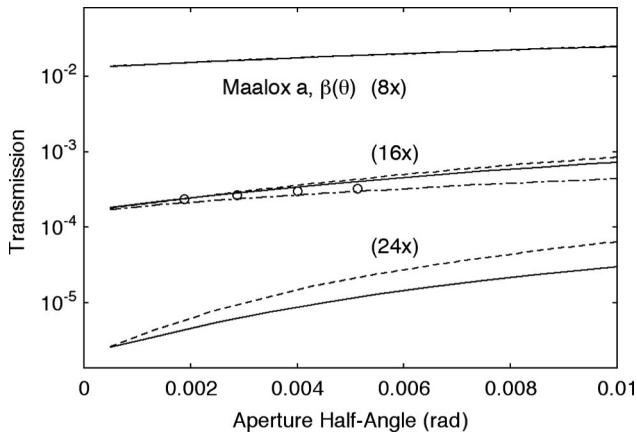


Fig. 4. Transmission calculated from Monte Carlo simulations for a 2 m path with different scaling of the Maalox absorption and volume scattering. Results are given for the experimental pipe geometry with perfectly absorbing cylindrical walls (solid curve) and with no walls (dashed curve). Calculated transmission for 16 $\times$  scaling with absorbing walls and with a reduced 0.1 rad half-angle field of view (dashed long-short) give better agreement with the experimental data (circles).

Monte Carlo simulations with  $10^8$  initial photons were performed for three water conditions based on the absorption and volume scattering functions of Maalox, scaled by 0.399 from the original measurements of Petzold [17], and further scaled by factors of 8 $\times$ , 16 $\times$ , and 24 $\times$ . The calculated transmission  $T(\theta)$  through an aperture at the end plane of the cylinder is shown in Fig. 4 as a function of aperture half-angle defined as aperture radius divided by 2 m. The transmission measured for the strongest scattering conditions [−36 dB extinction, Fig. 3(b)], at four iris settings is shown for comparison. We chose the 16 $\times$  Maalox scaling for  $\alpha$  and  $\beta(\theta)$  to have an approximate match to these conditions. The six calculated curves are for rays transmitted through the iris aperture within the full  $2\pi$  sr field of view, however the measured transmission was for a field of view limited by the distance and aperture of the integrating sphere (see Fig. 1). In the experiment, the integrating sphere collected light from any point in the iris aperture but within an  $\sim 0.01\pi$  sr field of view around a direction that varied slightly. An additional curve is shown for the calculated transmission in a fixed field of view of  $0.01\pi$  sr across the iris aperture. In the experiment, the field of view actually varied across the aperture, but this approximate calculation does give a better agreement with the measurements. In Fig. 4 it is apparent that the calculated transmission is nearly the same for the 5 cm radius pipe geometry as the unbounded (1 m radius) geometry for the 8 $\times$  and 16 $\times$  Maalox scale factors. However, with the stronger scattering conditions of the 24 $\times$  scaling, the absorbing walls of the pipe boundary significantly reduce transmission compared to the unbounded geometry. In the limit of small aperture, the transmission approaches the ballistic fraction, and this is independent of the radius of the cylindrical boundary condition.

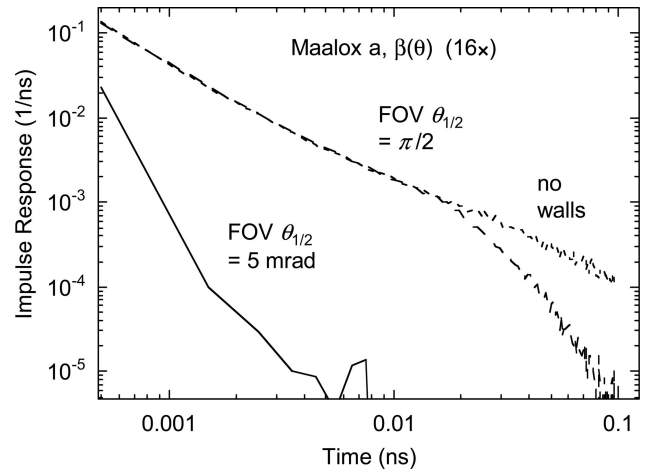


Fig. 5. Impulse response functions calculated from Monte Carlo simulations for a 2 m path with 16 $\times$  scaled Maalox absorption and volume scattering. The ballistic component has been removed and the collection aperture diameter is 20 mm. The results (solid curve) with 5 mrad half-angle field of view and absorbing walls are meant to match experimental conditions with the strongest scattering. Results with a full  $\pi/2$  half-angle field of view are shown with absorbing walls (long dash) and no walls (short dash).

Temporal information can be obtained from the Monte Carlo calculations at a much higher resolution than can be easily obtained experimentally. Impulse response functions from simulations with 16 $\times$  scaled Maalox absorption and volume scattering are shown in Fig. 5. The collection aperture diameter is 20 mm (5 mrad half-angle) in all cases, and the ballistic component, which contributes a delta function,  $1.48 \times 10^{-4} \delta(t)$ , is not present in the curves. One simulation was performed with absorbing cylindrical walls to approximate the experimental conditions. An impulse response was calculated for a 5 mrad half-angle field of view to match the lens and APD detector combination. Even with this large aperture, the response time is less than 1 ps, and it is clear why no pulse broadening was observed experimentally. The impulse response for the same conditions, except with a full  $\pi/2$  half-angle detector field of view, is considerably stronger and has a longer tail, but is still  $\ll 1$  ns. A second simulation with 1 m radius walls (effectively no wall boundary) was performed to understand the significance of the experimental pipe geometry and the effect of the walls. Evidently the walls suppress the response tail for times  $\geq 0.02$  ns, because photons with extended trajectories are prevented from reaching the detector. We should expect the response functions to diverge at times longer than a critical time  $t_c$  that represents the path difference between the ballistic path of length  $z = 2$  m and the shortest path, which just reaches the boundary, that is a symmetric path along the hypotenuse to the midpoint wall at radius  $r = 5$  cm:

$$t_c \approx \frac{n}{c} [(z^2 + 4r^2)^{1/2} - z] \approx 0.011 \text{ ns}, \quad (4)$$

where  $n = 1.34$  is the index of refraction for water and  $c$  is the speed of light. It is useful to consider how these impulse response functions would scale to longer ranges  $z$  if the products  $az$  and  $bz$  are kept constant. For example, at 32 m range with  $1 \times$  Maalox concentration, the response functions would be identical with these but with the time scaled by a factor of 16, giving response times that are still subnanoseconds. However, if the detector field of view is increased or displaced from the beam line the impulse response will broaden.

We also wish to explore the temporal behavior that could be expected with more realistic conditions in ocean water and for propagation over longer ranges. Additional Monte Carlo calculations were performed with the three ocean water types from [17], harbor, coastal ocean, and clear ocean, listed in Table 1. In a realistic communication link the source beam would likely have some initial divergence in order to alleviate pointing and tracking difficulties. We assume a small source with a beam centered on the receiver and with an angular profile  $p(\theta)$  that only depends on the angle  $\theta$  from this direction. We require the on-axis, time-dependent angular beam radiance at the receiver,  $L_B(\theta = 0, \mathbf{s}, t)$  (units of  $\text{sr}^{-1} \text{sr}^{-1} \text{ns}^{-1}$ ) where  $\mathbf{s}$  is the direction of light relative to  $\theta$ , the angular position of the photon at the receiver. The calculation is simplified because it is only necessary to generate the radiance at the receiver,  $L_0(\theta, \mathbf{s}, t)$ , from an on-axis source since  $L_B(\theta = 0, \mathbf{s}, t)$  is obtained from the convolution:

$$L_B(\theta = 0, \mathbf{s}, t) = \frac{\int_0^\pi p(-\theta) L_0(\theta, \mathbf{s}, t) \sin(\theta) d\theta}{\int_0^\pi p(\theta) \sin(\theta) d\theta}. \quad (5)$$

In these simulations,  $10^7$  photons were launched on axis, and data were compiled for trajectories passing through a spherical boundary centered at the source. The convolution in Eq. (5) was done for a source beam spread uniformly over a half-angle of 0.1 rad, which is a reasonable assumption since we are interested in a response that is an approximate average over some beam misalignment tolerance. Since the field of view of the receiver might be limited by focusing optics or the angular acceptance of spectral filters used to reduce background light, the beam impulse response  $u_B(t)$  was calculated by integrating the beam radiance over both a limited field of view with half-angle of 0.1 rad and the full  $\pi/2$  for comparison:

$$u_B(\theta = 0, t) = \int_{\text{FOV}} L_B(\theta = 0, \mathbf{s}, t) d\mathbf{s}. \quad (6)$$

We find it useful to characterize the propagation medium by a frequency response obtained from a Fou-

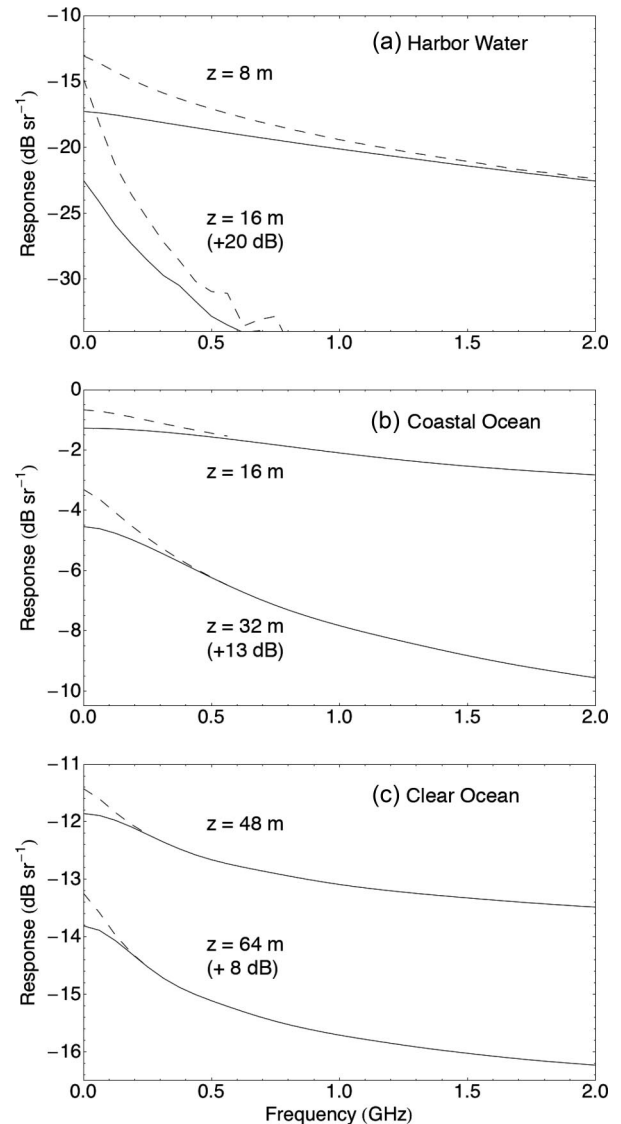


Fig. 6. Calculated frequency response in three different ocean waters at selected ranges for a source beam with uniform radiance over a 0.1 rad half-angle using absorption and scattering functions from [17]. The receiver is on axis and has a field-of-view half-angle of 0.1 (solid curve) and  $\pi/2$  (dashed curve).

rier transform of the impulse response function  $u_B(t)$ . These are shown in Fig. 6, normalized so that the value at zero frequency is given by  $u_B$  (units  $\text{sr}^{-1}$ ) equal to the integral of  $u_B(t)$  over time. If the source emits  $k$  photons in the solid angle  $\Omega = 0.01\pi \text{ sr}$ , the total number received in an aperture that subtends a solid angle  $\Delta\Omega$  would be given by  $ku_B\Delta\Omega$ , where  $\Delta\Omega \ll \Omega$ .

For each of the three ocean water types, results at two representative ranges are given. In all cases, the low frequency response is reduced with a limited field of view. At higher frequency, the response becomes less dependent on the field of view because more direct photon trajectories are involved. Harbor water has the highest level of absorption and scattering and presents the most difficult challenge for high band-



width communication. Even at the shortest range of 8 m, extinction is relatively high but the response at 1 GHz is reduced only 3 dB for the narrow field of view. At a range of 16 m, the extinction is severe and the 3 dB bandwidth is only  $\sim 100$  MHz. However in coastal water with the narrow field of view, the 3 dB bandwidth is  $>5$  GHz at 16 m range and  $\sim 880$  MHz at 32 m range, and in clear water, the 3 dB bandwidth is  $>5$  GHz at ranges up to 48 m.

These results indicate that high-bandwidth optical communication at  $\sim 1$  Gbit/s should not be limited by the propagation medium in a variety of ocean water types at moderate ranges. The simulations probably should be considered conservative because of the assumed large beam spread that allows more scattered photons to reach the receiver. A narrower source beam centered on the receiver would result in less temporal broadening and greater frequency bandwidth but at the cost of more critical pointing and tracking. On the other hand, if the receiver is misaligned from the beam direction, it will collect relatively more scattered photons and the temporal broadening will be increased.

#### 4. Summary

We have demonstrated optical communication at 1 Gbit/s through a 2 m water pipe with up to 36 dB of narrow-beam extinction ( $8.3$   $1/e$  lengths) obtained with suspensions of  $\text{Al}(\text{OH})_3$  and  $\text{Mg}(\text{OH})_2$ . The optical waveform at 532 nm was derived from a cw source at 1064 nm that was modulated in a 20 GHz EO modulator and frequency doubled in PPLN. The data rate was limited by the 1 GHz bandwidth APD detector, and we were not able to observe any evidence of temporal pulse broadening due to multiple scattering in the water path. The maximum water extinction, which still supported error-free transmission, was limited by the  $\sim 7$  mW average power generated by the optical source. Monte Carlo simulations of the propagation in the experimental geometry showed that no significant temporal broadening would be expected in agreement with these results. Simulations were also run for much longer propagation paths in three diverse ocean water types. The frequency response of the propagation medium was calculated from the Monte Carlo data, and these results indicated that in a range of ocean water conditions, there should be sufficiently high intrinsic bandwidth to support data rates greater than 1 Gbit/s over moderate ranges. Very high data rates should be useful in many applications that involve large quantities of data, such as image transfer or uploading of long-term stored sensor data, especially if the communication is done in a burst mode. To realize these applications, further work will be required to develop practical high-speed sources and detectors.

The authors thank Stephen Pappert and the Defense Advanced Research Projects Agency for supporting this work and Richard Bates for construction of the water pipe.

#### References

1. I. F. Akyildiz, D. Pompili, and T. Melodia, "Underwater acoustic sensor networks: research challenges," *Ad Hoc Networks* **3**, 257–279 (2005).
2. I. Vasilescu, K. Kotay, D. Rus, P. Corke, and M. Dunbabin, "Data collection, storage and retrieval with an underwater optical and acoustical sensor network," in *Proceedings of Sensys* (ACM, 2005), pp. 154–165.
3. R. W. Embley, W. W. Chadwick, E. T. Baker, D. A. Butterfield, J. A. Resing, C. E. J. de Ronde, V. Tunnicliffe, J. E. Lupton, S. K. Juniper, K. H. Rubin, R. J. Stern, G. T. Lebon, K. Nakamura, S. G. Merle, J. R. Hein, D. A. Wiens, and Y. Tamura, "Long-term eruptive activity at a submarine arc volcano," *Nature* **441**, 494–497 (2006).
4. R. Urlick, *Principles of Underwater Sound for Engineers*, 3rd ed. (Peninsula, 1996).
5. N. G. Jerlov, *Marine Optics*, Vol. 14 of Elsevier Oceanographic (Elsevier, 1976).
6. C. D. Mobley, *Light and Water: Radiative Transfer in Natural Waters* (Academic, 1994).
7. S. Karp, R. M. Gagliardi, S. E. Moran, and L. B. Stotts, in *Optical Channels: Fibers, Clouds, Water, and the Atmosphere* (Plenum, 1988), Chaps. 6 and 7.
8. J. W. Giles and I. N. Bankman, "Underwater optical communications systems. Part 2: basic design considerations," in *Proceedings of MILCOM 2005, IEEE Military Communications Conference* (IEEE, 2005), pp. 1700–1705.
9. B. Chochenour, L. Mullen, A. Laux, and T. Curran, "Effects of multiple scattering on the implementation of an underwater wireless optical communications link," in *Proceedings of IEEE Oceans 2006* (IEEE, 2006), p. 6.
10. N. Farr, A. Chave, L. Freitag, J. Preisig, S. White, D. Yoerger, and P. Titterton, "Optical modem technology for seafloor observatories," in *Proceedings of IEEE Oceans 2005* (IEEE, 2005), pp. 928–934.
11. J. B. Snow, J. P. Flatley, D. E. Freeman, M. A. Landry, C. E. Lindstrom, J. R. Longacre, and J. A. Schwartz, "Underwater propagation of high data rate laser communications pulses," *Proc. SPIE* **1750**, 419–427 (1992).
12. N. Farr, A. D. Chave, L. Freitag, J. Preisig, S. N. White, D. Yoerger, and F. Sonnichsen, "Optical modem technology for seafloor observatories," in *Proceedings of IEEE Oceans 2006* (IEEE, 2006), pp. 1–6.
13. R. E. Walker, *Marine Light Field Statistics* (Wiley, 1994), Eq. 2–2.6.
14. C. M. Blanca and C. Saloma, "Efficient analysis of temporal broadening of a pulsed focused Gaussian beam in scattering media," *Appl. Opt.* **38**, 5433–5437 (1999).
15. G. D. Boyd and D. A. Kleinman, "Parametric interaction of focused Gaussian light beams," *J. Appl. Phys.* **39**, 3597–3639 (1968).
16. A. Laux, R. Billmers, L. Mullen, B. Concannon, J. Davis, J. Prentice, and V. Contarino, "The abc's of oceanographic lidar predictions: a significant step toward closing the loop between theory and experiment," *J. Mod. Opt.* **49**, 439–451 (2002).
17. T. J. Petzold, "Volume scattering functions for selected ocean waters" (Scripps Institute of Oceanography, 1972), Paper SIO Reference 72–78.